

Spectro-polarimetry of GRB 180427A: evidence for distinct emission sites with varying polarisation

RUSHIKESH SONAWANE,^{1,2} SHABNAM IYYANI,^{2,1} SOUMYA GUPTA,³ TANMOY CHATTOPADHYAY,⁴ DIPANKAR BHATTACHARYA,⁵
VARUN. B. BHALERAO,⁶ SANTOSH V. VADAWALE,⁷ AND G. C. DEWANGAN⁸

¹*Centre for High Performance Computing, Indian Institute of Science Education and Research Thiruvananthapuram, Thiruvananthapuram, 695551, India*

²*School of Physics, Indian Institute of Science Education and Research Thiruvananthapuram, Thiruvananthapuram, 695551, India*

³*Homi Bhabha National Institute, Anushakti Nagar, Mumbai Maharashtra-400094, India*

⁴*Kavli Institute of Particle Astrophysics and Cosmology, Stanford University 452 Lomita Mall, Stanford, CA 94305, USA*

⁵*Department of Physics, Ashoka University, Sonapat, Haryana 131029, India*

⁶*Indian Institute of Technology Bombay, Mumbai, India*

⁷*Physical Research Laboratory, Ahmedabad, Gujarat 380009, India*

⁸*Inter-University Center for Astronomy and Astrophysics, Pune, Maharashtra 411007, India*

ABSTRACT

The dynamics of the origin of gamma-ray emissions in gamma-ray bursts (GRBs) remains an enigma. Through a joint analysis of GRB 180427A, observed by the Fermi Gamma-ray Space Telescope and AstroSat's Cadmium Zinc Telluride Imager, we identify emissions from two distinct regions with varying polarisation properties. Time-resolved polarisation analysis reveals a synchronous evolution of the polarisation angle (PA) and fraction (PF) with two emission pulses, peaking with a delay of 4.82 ± 0.12 s. Spectral analysis indicates that the first pulse is dominated by blackbody radiation, while the second pulse exhibits a non-thermal spectrum (power law with an exponential cutoff). Using a bottom-to-top approach through simulations, we decouple the polarisation properties of the individual spectral components, revealing polarisation fractions of 25% - 40% for the blackbody spectrum and 30% - 60% for the non-thermal spectrum. At a redshift of $z \sim 0.05$, the blackbody emission originates from the jet photosphere at 10^{11} cm, whereas the non-thermal emission arises from an optically thin region at 10^{15} cm. The changing dominance of these emissions explains the observed PA shift of $60^\circ \pm 22.3^\circ$. The spectral cutoff at 1 MeV suggests pair opacity due to the jet's low bulk Lorentz factor ($\Gamma \sim \text{tens}$). The high polarisation and hard spectral slopes ($\alpha > -0.5$) imply a top-hat jet structure observed off-axis, near the jet's edge. This off-axis viewing introduces anisotropy in the radiation within the viewing cone ($1/\Gamma$), accounting for the observed polarisation.

Keywords: Gamma-Ray Burst — Polarisation —(1868) — Interdisciplinary astronomy(804)

1. INTRODUCTION

Gamma-ray Bursts (GRBs) are among the most energetic transient phenomena in the universe. These bursts have been extensively studied by various space-based gamma-ray observatories, including the *Neil Gehrels Swift* observatory (Gehrels et al. 2004), the *Fermi* Gamma-ray Space Telescope (Meegan et al. 2009), and AstroSat's Cadmium Zinc Telluride Imager (CZTI, Rao et al. 2017). Understanding the nature of the prompt gamma-ray emission in GRBs through spectroscopy remains a significant challenge, often hindered by degeneracies where multiple spectral models fit the same data. Polarisation observations of GRB prompt emission are pivotal in breaking these degeneracies, as they provide insights into the radiation mechanisms, jet structure, and viewing geometry (Toma et al. 2009; Gill et al. 2021; Gill & Granot 2021). Notably, polarimetric observations of GRBs have been widely reported by *AstroSat* since 2015 (Vadawale et al. 2015) and POLAR between 2016–2018 (Produit et al. 2018). The integration of spectral data from *Fermi* with polarimetric measurements from AstroSat CZTI and POLAR are instruments in advancing our understanding of the GRB and its physics.

It has been observed that GRBs can exhibit intrinsic polarisation. Yet, time-averaged measurements may appear unpolarised due to a varying polarisation angle (Sharma et al. 2019; Burgess et al. 2019; Kole et al. 2020; Chattopadhyay et al. 2022; Gupta et al. 2024). Additionally, off-axis observations, especially with emissions consistent with photospheric, Compton-drag, or synchrotron emissions from random magnetic fields, can exhibit polarised signatures (Chand et al. 2018; Sharma et al. 2020). In this work, we present GRB 180427A as a case study demonstrating polarisation evolving synchronously with two emission pulses within a broadly fast-rise and exponential-decay (FRED) like light curve.

On April 27, 2018, the Gamma-ray Burst Monitor (GBM) aboard the *Fermi* Gamma-ray Space Telescope triggered at 10:37:03.04 UT (Fermi MET 546518228), detecting GRB 180427A at (R.A., decl.) = (283.33, 70.30) with a 1° uncertainty. The GBM light curve revealed a FRED-like pulse with a T_{90} duration of 26 seconds in the 50–300 keV range (Bissaldi 2018), and a fluence of $4.92 \pm 0.06 \times 10^{-5}$ erg cm $^{-2}$. Konus-Wind (Kozlova et al. 2018) and AstroSat CZTI (Sharma et al. 2018) also detected the burst, but no *Swift* BAT observations were recorded (Hurley et al. 2018). AstroSat CZTI measured a $T_{90} = 22.4$ s (40–200 keV) and recorded 981 Compton events (100–600 keV). No afterglow or redshift was reported for this burst.

The sections 2, 3, and 4 detail the light curve, spectral, and polarisation analyses, respectively, followed by a discussion in section 5.

2. LIGHTCURVE ANALYSIS

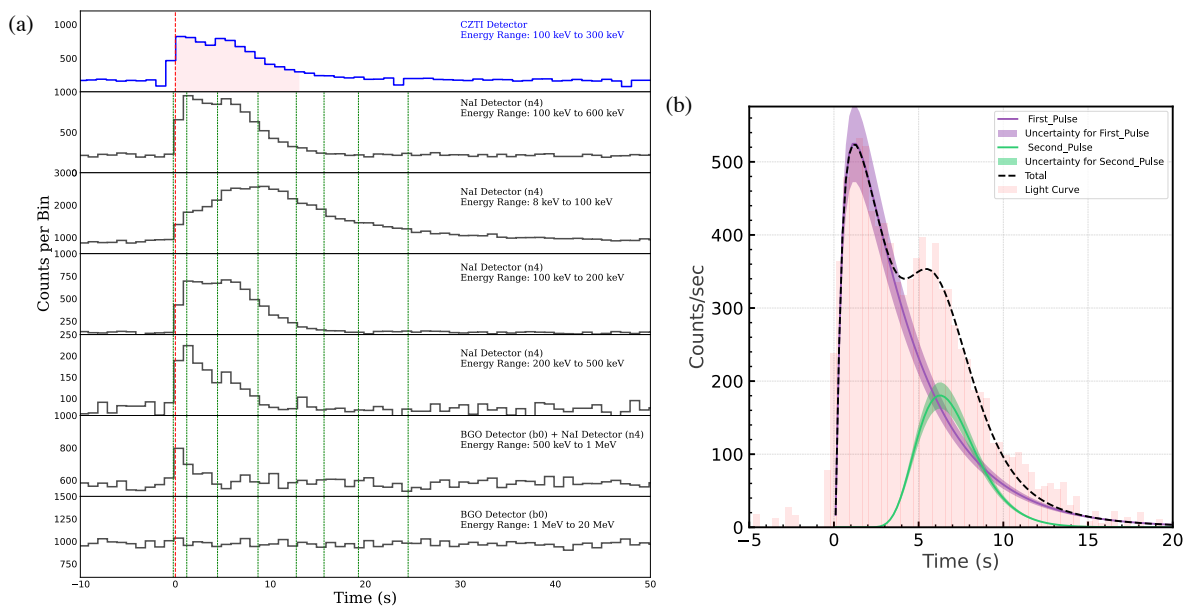


Figure 1. (a) The composite light curve of GRB 180427A is shown, with the top panel displaying the 100–300 keV single-event light curve from AstroSat CZTI. The pink-shaded region indicates the interval used for time-integrated polarisation analysis. The following panels show light curves from the *Fermi* NaI 4 and BGO 0 detectors, covering increasing energy ranges. The dashed red and green lines mark the *Fermi* GBM trigger time and the intervals for time-resolved spectral analyses, respectively. (b) The two peaks in the 100–600 keV light curve are modeled by Norris pulses (magenta and green curves), with shaded regions representing 68% confidence intervals. The pink histogram in the background shows the 0.37-second binned light curve for the same energy range.

Among the 12 sodium iodide (NaI) detectors and 2 bismuth germanate (BGO) detectors on the *Fermi* Gamma-ray Burst Monitor (GBM), only NaI4 (n4) was the brightest, positioned at an angle of less than 60° , while BGO0 (b0) was the brightest BGO detector. These were utilised for the analysis. The burst exhibited a single-pulse, fast-rise exponential decay (FRED) light curve, as shown in Figure 1a. The composite light curve spans a broad energy range from 8 keV to 20 MeV. The top panel displays the single-event light curve from AstroSat CZTI in the 100–300 keV range, with the shaded pink region indicating the time interval used for time-integrated polarisation analysis. Both

AstroSat CZTI (100-300 keV) and *Fermi* GBM (100-600 keV) light curves shown in the top two panels respectively in Figure 1a exhibit two distinct peaks. No significant emission was observed above 1 MeV in the BGO0 detector, suggesting a spectral cutoff at higher energies.

The *Fermi* background subtracted light curve binned in 0.37s in the 100-600 keV range was analysed using a model comprising two Norris emission pulses (Norris et al. 2005). A Norris emission pulse is given by:

$$I(t) = K \exp\left(-\frac{\tau_1}{t} - \frac{t}{\tau_2}\right) \quad (1)$$

where K is the normalisation constant, τ_1 is the rise time, and τ_2 is the decay time after the pulse maximum. The model was fitted to the light curve using the Maximum Likelihood Estimation (MLE) method in the 3ML software (Vianello et al. 2015), yielding a reduced chi-square of 0.72. The two emission pulses are shown in Figure 1b as magenta and green curves. The total model, formed by combining the two pulses, is shown by the dashed black curve, which closely matches the two observed peaks in the light curve (100–600 keV), depicted in pink in the background of Figure 1b. The shaded regions around the curves represent the 68% uncertainty level of model derived from the fit.

A cross-correlation analysis was performed between the obtained Norris pulses, using a time binning of 0.37 seconds over the interval [0.5, 10] seconds. Multivariate sampling of the best-fit values incorporating the covariance matrix was performed, simulating nearly 10^5 instances of the Norris pulses and estimated the time delay for each simulation. The mean and standard deviation of the time delay distribution are $t_{\text{delay}} = 4.84 \pm 0.12$ s. The distinct emission pulses, peaking at different times, suggest the emissions originate from separate sites within the GRB jet. Further examination of their spectral composition is essential, which is presented in the next section 3.

3. SPECTRAL ANALYSIS

The time-integrated and time-resolved spectroscopy of the burst were performed using *Fermi* GBM data in the Multi-Mission Maximum Likelihood (3ML) software. The spectral parameters were estimated via the maximum likelihood estimation method, with the Akaike Information Criterion (AIC, Akaike 1974) applied to select the best-fitting model.

For time-integrated spectral analysis, the time interval identified to encompass the full burst emission is [-2, 45] seconds. The burst was best modeled using the Band function (Band et al. 1993) alone, which provided the lowest AIC value. The resulting Band function parameters are: low-energy power-law index $\alpha = -0.54 \pm 0.05$, peak energy $E_{\text{peak}} = 110 \pm 3.4$ keV, and high-energy power-law index $\beta = -2.61 \pm 0.07$. The total burst fluence was found to be 6.25×10^{-5} erg/cm².

For time-resolved spectroscopy, the light curve from the brightest NaI detector (n4) was binned using the Bayesian Block binning method, with a false alarm probability of $p_0 = 0.01$ (Scargle et al. 2013). This method optimally segments the data into blocks where no significant variation from a constant rate is observed. As Bayesian blocks do not ensure a sufficient signal-to-noise ratio in each bin, we combined several bins during the main burst emission and excluded bins beyond 25 seconds due to their very low signal-to-noise ratio. This process resulted in seven time intervals with adequate signal-to-noise ratios for constraining the spectral parameters, as illustrated in Figure 1a. The Band function alone provided the best fit for all intervals. The temporal evolution of spectral parameters is depicted in Figure 2a, where the photon index α is steeper than the "line of death" for synchrotron emission ($\alpha = -0.67$), suggesting a potential thermal component.

The light curve showed two distinct emission pulses, indicating the presence of two emission sites and thereby two spectral components. To explore this further, we analysed the spectrum using two-component models: blackbody (BB) + Band and BB + cutoff power-law (CPL). Both models resulted in random residuals with $\Delta AIC \leq 5$. Following Occam's Razor rule, the BB + CPL model was preferred due to fewer spectral parameters and the steep β of the Band function, which aligns with the absence of emission above 1 MeV, as observed in the light curve. The temporal evolution of the spectral parameters, including power-law index, spectral cutoff energy (E_c), and blackbody temperature (kT), is shown in Figure 2b. The νF_ν plot for the BB + CPL model, derived from one of the brightest time bins, is shown in Figure 2c. The shaded region represents the 68% uncertainty level of the spectral model shape derived from the fit.

To examine the spectral composition of the emission pulses, we estimated the temporal evolution of the photon flux for both the BB and CPL components across different energy ranges, as shown in Figure 2d. In the 100–600 keV range (top panel of Figure 2d), the BB component initially dominates over the CPL, but as time progresses, the CPL emission becomes more dominant. Comparing this with the 100–600 keV light curve (Figure 1b), we find that both emission pulses contain contributions from both components. The first pulse is primarily driven by the BB component,

while the second pulse is dominated by the CPL. In the 100–220 keV range, the BB component’s dominance becomes more pronounced, with higher-energy contributions from the CPL being confined to energies above those of the BB component (Figure 2c).

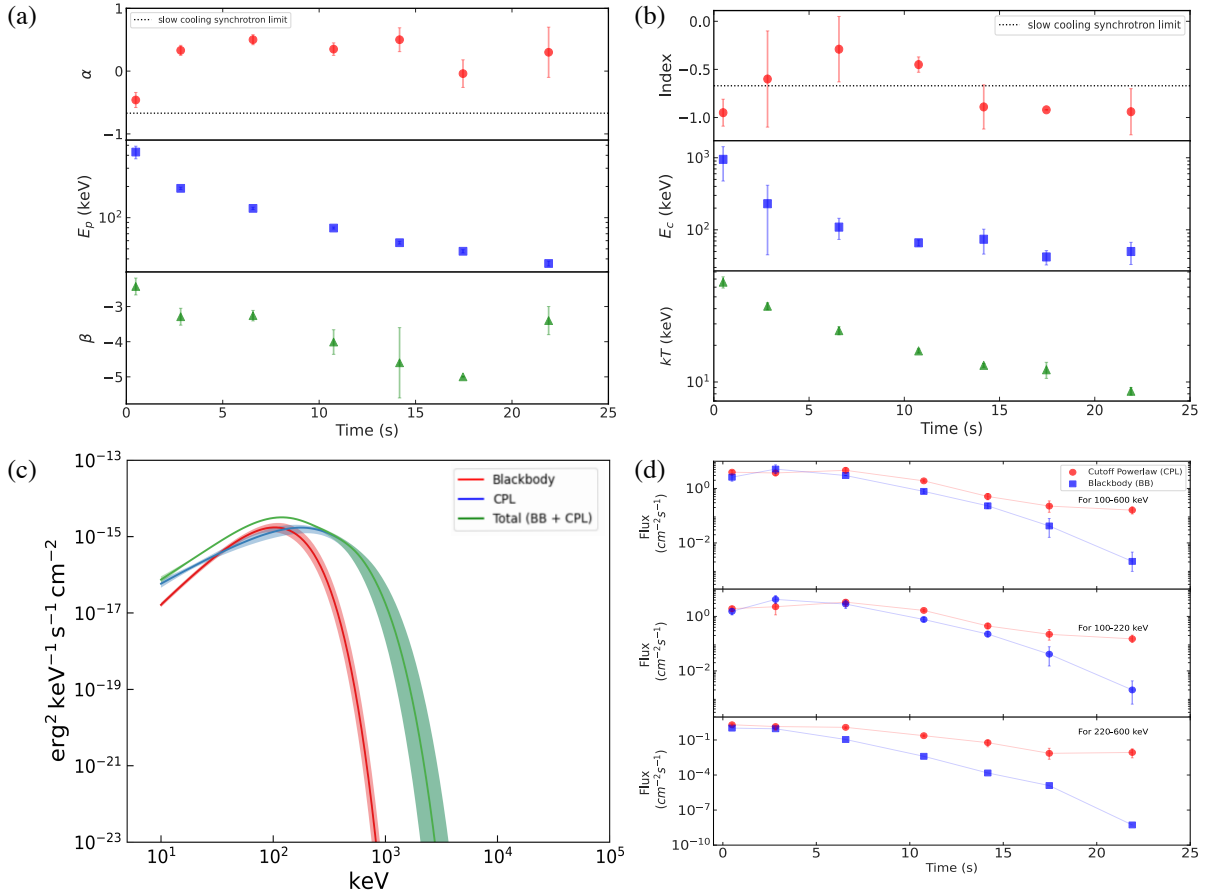


Figure 2. The temporal evolution of spectral parameters for (a) the Band function and (b) the Blackbody + Cutoff-powerlaw (BB + CPL) models is presented. For the Band function, the parameters α , E_p , and β are shown in the upper, middle, and lower panels using red circles, blue squares, and green triangles, respectively. For the BB + CPL model, the power-law index, cutoff energy, E_c , and blackbody temperature, kT are displayed similarly in the upper, middle, and lower panels. The dotted line in the α and Index plots indicates the expected low-energy power-law index (-0.67) for slow-cooled synchrotron emission. (c) The νF_ν plot of the BB + CPL model obtained for one of the brightest bins (1.2 - 4.4 s) is shown. (d) The temporal evolution of photon flux for the BB (blue squares) and CPL (red circles) components is shown across three energy ranges—100–600 keV, 100–220 keV, and 220–600 keV—in the upper, middle, and lower panels, respectively.

4. POLARISATION ANALYSIS

AstroSat CZTI is equipped to conduct polarisation studies in the energy range of 100–600 keV using the Compton polarimetry technique. The polarisation measurement methodology follows the detailed procedure described in [Chatopadhyay et al. 2022](#), which was applied in this work. The methodology is briefly described in Appendix A. The obtained azimuthal Compton count distribution was modeled using the cosine function in equation A1, with Bayesian analysis employing Markov Chain Monte Carlo (MCMC) methods in PyMC3¹. The posterior distributions for the polarisation fraction (PF) and polarisation angle (PA) were filtered to remove values where PF exceeded 100%. The refined distributions were used to generate corner plots for PF and sky PA. The reported PF and PA values correspond to the most probable values from these posterior distributions. Notably, the PA posterior distribution in this work

¹ <https://pypi.org/project/pymc3/>

showed a shoulder in addition to the primary peak. This feature is attributed to the large error bars in the azimuthal distribution (see Appendix A for further discussion). The reported PA value is derived from the most probable peak of the PA posterior distribution, modeled with a Gaussian function. The standard deviation of this fit is used as the 68% credible region for PA, while the 68% credible region for PF is directly taken from its posterior distribution.

We adopt the null hypothesis as unpolarised radiation, represented by a straight line, and the alternate hypothesis as polarised radiation, modeled by a cosine function. The presence of polarisation, or the strength of evidence supporting the alternate hypothesis, is evaluated using the Bayes factor. To interpret the evidence grade in favour of the alternate hypothesis, we employ the Kass and Raftery’s modified Jeffrey’s scale (Kass & Raftery 1995).

Initially, we performed polarisation analysis on the time-integrated burst region, spanning 0 to 13 seconds, during which approximately 1020 Compton events were detected. The emission was found to be polarised, with a Bayes factor = 19.8 and $\Delta\text{WAIC} = -15$ (Watanabe 2010), indicating positive evidence for polarisation. The polarisation fraction was measured as $\text{PF} = 60.06 \pm 20.40\%$, and the sky PA was $45.45 \pm 9.86^\circ$ (Detector PA = $25 \pm 9.86^\circ$). The reported errors also account for the systematic errors mentioned in Chattopadhyay et al. (2019) and Sharma et al. (2019). Figure 3a presents the corner plot of the posterior distributions for PF and sky PA, alongside the azimuthal distribution and the most probable modulation curve.

To investigate the temporal evolution of polarisation properties, we performed a sliding window analysis with a 4-second window, incremented by 1 second. The resulting temporal variations in PF and PA are shown in the second and third panels of Figure 3b. The PA in the detector plane shifted from negative to positive values over time, with the PF constrained between 60% and 80% at a 68% credible region for one parameter of interest. The Bayes factor for each interval ranged between 2 and 3.2. Interestingly, the change in PA occurred around 4.5 seconds, which corresponds to the time delay between the peaks of the two emission pulses identified in the GRB light curve.

To achieve more statistically significant results and confirm this variation, we conducted a time- and energy-resolved polarisation analysis. Spectral analysis revealed that the first pulse is dominated by blackbody emission, particularly in the energy range 100–220 keV (Figure 2d). Based on the sliding window and spectral analysis, we divided the Compton light curve into two intervals: 0–3 seconds and 4.5–9 seconds, with energy ranges 100–220 keV and 100–600 keV, respectively (Figure 3b). For the second pulse, where the CPL component dominates, we were unable to conduct the energy resolved analysis above 220 keV due to insufficient Compton events. The analysis identified polarised emission in both intervals, with Bayes factor 5 and 10, and ΔWAIC values of -5.49 and -12, respectively indicating a positive evidence for polarisation. The corner plots of the posterior distributions for PF and sky PA obtained for these temporal and energy-resolved regions, along with the azimuthal distributions and the most probable modulation curves, are shown in Figures 3c and 3d. The most probable PA in the detector plane shifted from $-27.1 \pm 8.9^\circ$ to $+25.27 \pm 11.1^\circ$, aligning with the temporal evolution of the two emission pulses observed in the light curve. This confirms that both spectral components (blackbody in the first pulse and cutoff power-law in the second pulse) are polarised but with different polarisation angles.

Although the Bayes factor of > 3.2 in each case confirms the presence of polarised radiation, we were unable to independently constrain the polarisation fraction of the BB and CPL components, as both are present throughout the emission pulses. Nonetheless, the spectral and polarisation analyses provides the following insights:

- When the BB component dominates, the net PA in the detector plane is negative, and when the CPL component dominates, the net PA is positive.
- As the dominance of the spectral components shifts over time, the PA in the detector plane transitions from negative to positive.
- The change in PA in the detector plane, ΔPA , over time is $60 \pm 22.25^\circ$.
- The flux ratio of BB to CPL in the first interval (0–3 seconds) is 1.79 in the 100–220 keV range.
- In the CPL-dominated second interval (4.5–9 seconds), the flux ratio becomes 0.45 in the 100–600 keV range.

Additionally, according to Lundman et al. 2014, the maximum observable polarisation fraction for thermal emission viewed off-axis is limited to 40% (Gill et al. 2021).

To estimate the individual polarisation fractions of the components, we performed simulations combining the two spectral components (CPL and BB) with different polarisation fractions while keeping the polarisation angles fixed at their most probable values derived from observational analysis. We tested various combinations reflecting the observed

flux ratios of each component. The posterior distributions of PA from each simulation were analysed, and the possible combinations of polarisation fractions for the BB and CPL components were constrained to align with the observed polarisation properties (refer Appendix B). This simulation approach yields polarisation fractions for blackbody and cutoff power-law emissions in the ranges of 25%–40% and 30%–60%, respectively.

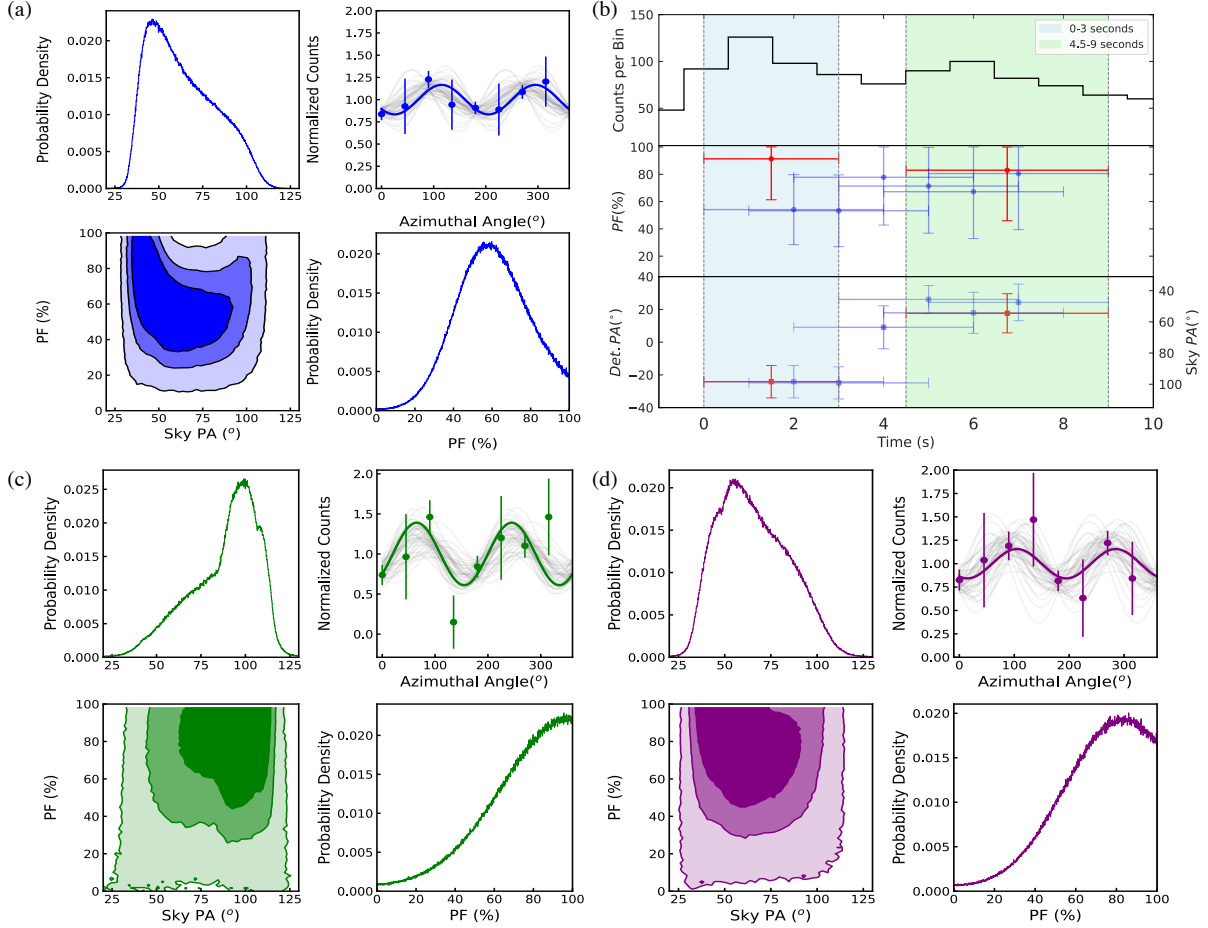


Figure 3. (a) The 2D histogram of PF and Sky PA are shown for time-integrated polarisation analysis (0–13 s, 100–600 keV). (b) The top panel shows the Compton light curve from AstroSat CZTI in the 100–600 keV range. The middle and bottom panels display the polarisation fraction (blue circles) and detector polarisation angle (blue squares) from a sliding window analysis with 4 s bins and 1 s steps. The second y-axis in the bottom panel represents the corresponding sky polarisation angles. The time and energy resolved polarisation windows (0–3 s; 100–220 keV and 4.5–9 s; 100–600 keV) are shaded in blue and green, with the obtained PF and PA values shown in red circles and squares respectively. The 2D histograms of PF and Sky PA are shown for: (c) time and energy-resolved (0–3 s, 100–220 keV), and (d) time-resolved (4.5–9 s, 100–600 keV) in green, and purple corner plots, respectively. The contour lines in the 2D histograms represent 68%, 95%, and 99% credible regions for two parameters of interest. Each plot includes the most probable modulation curve (solid line) and 1000 randomly selected modulation curves (shaded grey lines) from MCMC simulations in the top right. The obtained posterior distributions for PF and PA are shown in the bottom right and top left panels, respectively in each plot.

5. DISCUSSION & SUMMARY

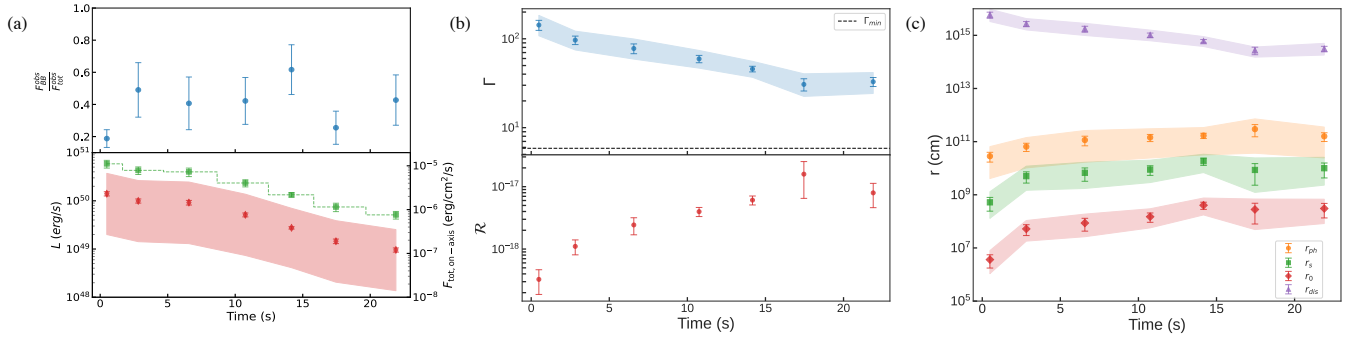


Figure 4. The temporal evolution of the jet’s outflow dynamics, based on the observed thermal component, is presented. (a) The ratio of observed blackbody flux to total flux, $F_{BB}^{obs}/F_{tot}^{obs}$, is depicted in blue circles in the upper panel. In the lower panel, the burst luminosity L (for a redshift $z = 0.05$) is shown in red diamonds, while the total flux $F_{tot,on-axis}^{obs}$ expected on-axis is plotted on the second y-axis in green square. (b) The evolution of the bulk Lorentz factor (Γ) and the expected Γ_{min} are plotted in blue circles and a dashed black line, respectively, in the upper panel. The lower panel shows the evolution of \mathcal{R} (red circles) over time. (c) The temporal evolution of key radii—nozzle radius (r_0), saturation radius (r_s), photospheric radius (r_{ph}), and dissipation radius (r_d)—are plotted using red diamonds, green squares, orange circles, and purple triangles, respectively. The shaded regions in all three plots (a, b, and c) indicate the upper and lower limits corresponding to redshift values ranging from $z = 0.03$ to 0.09 .

The presence of a prominent thermal component, contributing approximately $F_{BB}^{obs} \sim 20\%$ to 60% of the total observed flux, F_{tot}^{obs} , throughout the burst (Figure 4a), along with the hard spectral slopes ($\alpha > -0.5$) (Figure 2a), points to photospheric emission and a baryon-dominated outflow (Acuner et al. 2019, 2020). The non-thermal emission (CPL) is then attributed to an optically thin dissipation site, as indicated by the observed time delay, t_{delay} , between the two emission pulses revealed through light curve and spectral analyses. In such cases, both blackbody (BB) and cutoff power-law (CPL) components are expected to be unpolarised when viewed on-axis, regardless of whether the CPL arises from synchrotron emission or inverse Compton scattering. Therefore, the observed polarisation indicates a strong anisotropy of radiation within the observed view cone of $1/\Gamma$ where Γ is the bulk Lorentz factor (Toma et al. 2009; Chand et al. 2018; Gill et al. 2021).

In the structured jet model, the luminosity and bulk Lorentz factor decrease with the angle measured from the jet axis. When the jet is viewed off-axis, the spectrum is expected to appear softer due to reduced Doppler boosting and lower luminosity (Lundman et al. 2013, 2014). However, in the case of GRB 180427A, the observed hard α , combined with the high polarisation, suggests a top-hat jet structure with the burst being viewed near the jet’s edge. Such a configuration can result in polarisation of both the BB and CPL components, arising from the anisotropy of radiation within the viewing cone of $1/\Gamma$ along the jet edge (Waxman 2003; Toma et al. 2009).

By adopting a top-hat jet model, neglecting high-latitude emissions, and assuming an active central engine throughout the burst, the thermal component enables us to estimate the outflow parameters using the methodology outlined in Pe’er et al. 2007; Iyyani et al. 2013. Notably, the calculations in Pe’er et al. 2007 are based on the assumption of on-axis viewing. However, since we assume the burst is observed along the edge of the top-hat jet, the flux within the viewing cone will be reduced to half of what it would be for an on-axis view. Consequently, to apply the equations from Pe’er et al. 2007, the energy fluxes (both the blackbody and total fluxes) are redefined as twice the observed values. The corresponding total flux ($F_{tot,on-axis}^{obs}$) is displayed in the lower panel of Figure 4a. These values are utilised to calculate the burst luminosity, L , and determine the outflow parameters.

The dissipation radius is estimated as $r_{dis} = 2\Gamma^2 ct_{delay}$ where c is the speed of light. Given that the dissipation radius (r_{dis}) is of the order of 10^{15} cm or smaller, and the nozzle radius (r_0) of the jet exceeds 10^6 cm, we estimate the burst redshift to be between $z = [0.03 - 0.09]$. Assuming a radiation efficiency of 50% (Racusin et al. 2009; Racusin et al. 2011) and applying the Λ_{CDM} cosmology with $H_0 = 67.4 \pm 0.5 \text{ km s}^{-1} \text{ Mpc}^{-1}$, $\Omega_m = 0.315$, and $\Omega_{vac} = 0.685$ (Aghanim et al. 2020), the luminosity, L (Figure 4a, lower panel), \mathcal{R} (Figure 4b, lower panel) and outflow parameters (Figures 4b and c) are estimated. For $z = 0.05$, the luminosity decreases from 1.4×10^{50} erg/s to 9.5×10^{48} erg/s over time. The Γ decreases from 143 to 31 (Figure 4b), consistent with recent findings by Dereli-Bégué et al. 2022 of lower values of Γ . The high-energy cutoff in the CPL component could be due to pair production as a result of lower Γ .

Using this cutoff, the minimum Lorentz factor in the optically thin region is estimated as $\Gamma_{\min} = 5.86$ (Lithwick & Sari 2001).

The evolution of key outflow radii, such as the nozzle radius (r_0), saturation radius (r_s), and photospheric radius (r_{ph}), is shown in Figure 4c. For $z = 0.05$, r_{ph} averages around 1.3×10^{11} cm while dissipation radius r_{dis} is around 1.8×10^{15} cm. The nozzle radius evolves from 3.6×10^6 cm to 3×10^8 cm while r_s is around 8.3×10^9 cm. These trends align with previous studies (Iyyani et al. 2013, 2016).

In summary, the spectro-polarimetric analysis of GRB 180427A identifies two distinct emission components originating from different regions within the baryon-dominated outflow, observed off-axis near the edge of the top-hat jet. The light curve and spectral analyses indicate a time delay between two emission pulses dominated by blackbody radiation from the photosphere (at $\sim 10^{11}$ cm) and CPL emission from the optically thin region (at $\sim 10^{15}$ cm) respectively. The relatively low bulk Lorentz factor causes these emissions to appear as separate peaks in the light curve, with a delay of approximately 5 seconds. The temporal variation in the dominance of these emissions results in changes to the observed polarisation angle, highlighting their distinct polarisation properties.

ACKNOWLEDGMENTS

We express our gratitude to Prof. Felix Ryde and Prof. A. R. Rao for their enlightening discussions and invaluable insights. This publication utilizes data from the AstroSat mission, operated by the Indian Space Research Organisation (ISRO), and archived at the Indian Space Science Data Centre (ISSDC). The CZT-Imager was developed through a collaborative effort involving multiple institutes in India, including the Tata Institute of Fundamental Research (TIFR), Mumbai; the Vikram Sarabhai Space Centre, Thiruvananthapuram; the ISRO Satellite Centre (ISAC), Bengaluru; the Inter-University Centre for Astronomy and Astrophysics (IUCAA), Pune; the Physical Research Laboratory, Ahmedabad; and the Space Applications Centre, Ahmedabad. This research also incorporates data from the Fermi mission, accessed via the High Energy Astrophysics Science Archive Research Center (HEASARC) Online Service provided by NASA's Goddard Space Flight Center. Additionally, the Geant4 simulations presented in this paper were conducted using the high-performance computing resources at the Inter-University Centre for Astronomy and Astrophysics (IUCAA). S.I. is supported by the DST INSPIRE Faculty Scheme (IFA19-PH245) and SERB SRG grant (SRG/2022/000211).

APPENDIX

A. DOUBLE HUMPED POSTERIOR OF POLARISATION ANGLE

AstroSat CZTI conducts polarisation study in the energy range of 100 - 600 keV using Compton polarimetry technique. When polarised photons incident on the detector scatter, they tend to scatter perpendicularly to their electric field vector. A Compton polarimeter analyses the azimuthal distribution of these scattered photons. This distribution is modeled using a cosine function of the form:

$$C(\phi) = A \cos \left[2 \left(\phi - \phi_0 + \frac{\pi}{2} \right) \right] + B \quad (\text{A1})$$

where ϕ_0 is the polarisation angle (PA) of the incident photons as measured in the CZTI detector plane, A/B is the modulation factor (μ), and ϕ represents the azimuthal angle. The polarisation fraction (PF) is calculated by normalising the modulation (μ) with μ_{100} , which is the modulation factor for 100% polarised emission incident on the detector from the same direction as the GRB, with the same spectrum and detected PA. The detector plane PA is then converted to the sky PA in the sky reference frame, taking into account the satellite's orientation.

The methodology for polarisation measurement presented in this work follows the detailed description in Chatopadhyay et al. 2022. The Compton events for the burst is selected based on Compton kinematics and adjacent pixel criteria. The azimuthal distribution is then background-subtracted using the combined distributions of Compton events from the pre- ($T_0 - 503$ to $T_0 - 83$) and post-GRB ($T_0 + 97$ to $T_0 + 407$) regions. This background-subtracted distribution is then geometrically corrected by normalising it with the azimuthal distribution from simulations, where unpolarised GRB emission with the same spectrum and incident angle was used. Finally, the azimuthal distribution is modeled with a cosine function, as described in the equation A1, using Bayesian analysis technique.

AstroSat’s mass model is simulated using the Geant4 toolkit (Agostinelli et al. 2003), which includes detailed geometries for all the payload and the satellite bus (Chattopadhyay et al. 2019; Mate et al. 2021). The study of polarisation of off-axis sources are challenging, as the polarisation properties can be altered due to interactions with other payload components and the CZTI housing elements. By conducting a Geant4 simulation, we can trace each photon as it interacts with the detector, allowing for a more accurate analysis of its polarisation characteristics.

Geant4 simulations were performed to investigate the double-humped posterior distributions of the polarisation angle observed in the data analysis of GRB 180427A. The simulations incorporated spectral information to direct photons from both the blackbody (BB) and cutoff power-law (CPL) components onto the detector. In total, 8×10^5 photons were simulated to interact with the detector. For instance, we considered the scenario of BB-to-CPL photon flux ratio of 0.45. The BB and CPL components were assigned polarisation fractions of 30% and 60%, respectively, with polarisation angles in the sky plane of $106.68 \pm 2^\circ$ (detector PA = $-32 \pm 2^\circ$) and $42.57 \pm 2^\circ$ (detector PA = $28 \pm 2^\circ$).

Due to the large number of simulated photons, the number of Compton scattering events detected was approximately 10^4 . This resulted in a modulation curve with significantly reduced statistical errors (Figure Aa). Analysis of this modulation curve yielded a posterior distribution for the detector polarisation angle (PA) that was single-peaked, as shown in the upper-left corner of Figure Aa. To account for the larger error bars observed in real data, we systematically increased the error bars on the simulated modulation curve to match the observational uncertainties. Interestingly, as the error bars grew, the resultant PA posterior developed a shoulder to the most probable peak, closely resembling the observed double-humped distribution. Meanwhile, the posterior of the polarisation fraction (PF) remained single-peaked but with increased standard deviations. These results, thus, suggest that the double-humped distribution of PA obtained from the observed data analysis is a consequence of the larger error bars associated with the observed modulation curve.

B. CONSTRAINING PF OF EMISSION COMPONENTS

The presence of both spectral components during the emission pulses complicates the complete decoupling of their individual polarisation properties through modulation curve analysis. To address this, we performed simulations following the methodology outlined in Appendix A of this section, using the Geant4 simulation framework described therein.

For a given combination of polarisation fractions (PFs) of the blackbody (BB) and cutoff power-law (CPL) components, we examined scenarios where the BB-to-CPL photon flux ratio varied. When CPL dominated, the net detector polarisation angle (PA) remained positive, while in cases where BB dominated, the net PA became negative, changing by $\Delta\text{PA} = 60 \pm 22.25^\circ$. Additionally, theoretical models such as Lundman et al. 2014 suggest that the BB emission is expected to exhibit a maximum polarisation fraction of 40%. We systematically explored various PF combinations for BB and CPL, ranging from 20% to 40% and 20% to 70%, respectively, in increments of 5%. PF combinations that satisfied the above mentioned observational constraints were identified as plausible values for the respective components. Consequently, we constrained the PF of the blackbody component to lie within 25% – 40%, while the CPL component’s PF was determined to range from 30% – 60%.

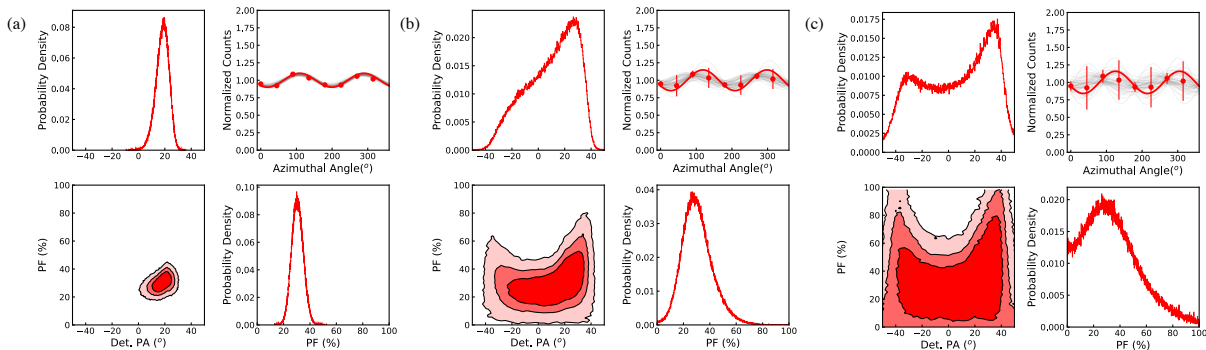


Figure 5. The results of the polarisation analysis for various cases are presented, where the errors on the simulated modulation data points are (a) low, (b) moderately high, and (c) relatively large (comparable to the observations). For each case, the posterior distributions of the polarisation angle (PA) and polarisation fraction (PF), along with the corresponding 2D histograms with contour lines corresponding to 68%, 95% and 99% credible regions for two parameters of interest are shown.

REFERENCES

- Acuner, Z., Ryde, F., Pe'er, A., Mortlock, D., & Ahlgren, B. 2020, *ApJ*, 893, 128, doi: [10.3847/1538-4357/ab80c7](https://doi.org/10.3847/1538-4357/ab80c7)
- Acuner, Z., Ryde, F., & Yu, H.-F. 2019, *MNRAS*, 1306, doi: [10.1093/mnras/stz1356](https://doi.org/10.1093/mnras/stz1356)
- Aghanim, N., Akrami, Y., Ashdown, M., et al. 2020, *A&A*, 641, A6, doi: [10.1051/0004-6361/201833910](https://doi.org/10.1051/0004-6361/201833910)
- Agostinelli, S., et al. 2003, *Nucl. Instrum. Meth. A*, 506, 250, doi: [10.1016/S0168-9002\(03\)01368-8](https://doi.org/10.1016/S0168-9002(03)01368-8)
- Akaike, H. 1974, in *Selected Papers of Hirotugu Akaike* (Springer), 215–222
- Band, D., Matteson, J., Ford, L., et al. 1993, *ApJ*, 413, 281, doi: [10.1086/172995](https://doi.org/10.1086/172995)
- Bissaldi, E. 2018, *GRB Coordinates Network*, 22678, 1
- Burgess, J. M., Kole, M., Berlato, F., et al. 2019, *A&A*, 627, A105, doi: [10.1051/0004-6361/201935056](https://doi.org/10.1051/0004-6361/201935056)
- Chand, V., Chattopadhyay, T., Iyyani, S., et al. 2018, *ApJ*, 862, 154, doi: [10.3847/1538-4357/aacd12](https://doi.org/10.3847/1538-4357/aacd12)
- Chattopadhyay, T., Vadawale, S. V., Aarthy, E., et al. 2019, *ApJ*, 884, 123, doi: [10.3847/1538-4357/ab40b7](https://doi.org/10.3847/1538-4357/ab40b7)
- Chattopadhyay, T., Gupta, S., Iyyani, S., et al. 2022, *ApJ*, 936, 12, doi: [10.3847/1538-4357/ac82ef](https://doi.org/10.3847/1538-4357/ac82ef)
- Dereli-Bégué, H., Pe'er, A., Ryde, F., et al. 2022, *Nature Communications*, 13, 5611, doi: [10.1038/s41467-022-32881-1](https://doi.org/10.1038/s41467-022-32881-1)
- Gehrels, N., Chincarini, G., Giommi, P., et al. 2004, *The Astrophysical Journal*, 611, 1005
- Gill, R., & Granot, J. 2021, *MNRAS*, 504, 1939, doi: [10.1093/mnras/stab1013](https://doi.org/10.1093/mnras/stab1013)
- Gill, R., Kole, M., & Granot, J. 2021, *Galaxies*, 9, 82, doi: [10.3390/galaxies9040082](https://doi.org/10.3390/galaxies9040082)
- Gupta, R., Pandey, S. B., Gupta, S., et al. 2024, *ApJ*, 972, 166, doi: [10.3847/1538-4357/ad5a92](https://doi.org/10.3847/1538-4357/ad5a92)
- Hurley, K., Mitrofanov, I. G., Golovin, D., et al. 2018, *GRB Coordinates Network*, 22679, 1
- Iyyani, S., Ryde, F., Burgess, J. M., Pe'er, A., & Bégué, D. 2016, *MNRAS*, 456, 2157, doi: [10.1093/mnras/stv2751](https://doi.org/10.1093/mnras/stv2751)
- Iyyani, S., Ryde, F., Axelsson, M., et al. 2013, *MNRAS*, 433, 2739, doi: [10.1093/mnras/stt863](https://doi.org/10.1093/mnras/stt863)
- Kass, R. E., & Raftery, A. E. 1995, *Journal of the American Statistical Association*, 90, 773, doi: [10.1080/01621459.1995.10476572](https://doi.org/10.1080/01621459.1995.10476572)
- Kole, M., De Angelis, N., Berlato, F., et al. 2020, *A&A*, 644, A124, doi: [10.1051/0004-6361/202037915](https://doi.org/10.1051/0004-6361/202037915)
- Kozlova, A., Golenetskii, S., Aptekar, R., et al. 2018, *GRB Coordinates Network*, 22680, 1
- Lithwick, Y., & Sari, R. 2001, *The Astrophysical Journal*, 555, 540
- Lundman, C., Pe'er, A., & Ryde, F. 2013, *MNRAS*, 428, 2430, doi: [10.1093/mnras/sts219](https://doi.org/10.1093/mnras/sts219)
- . 2014, *MNRAS*, 440, 3292, doi: [10.1093/mnras/stu457](https://doi.org/10.1093/mnras/stu457)
- Mate, S., Chattopadhyay, T., Bhalerao, V., et al. 2021, *Journal of Astrophysics and Astronomy*, 42, 93, doi: [10.1007/s12036-021-09763-x](https://doi.org/10.1007/s12036-021-09763-x)
- Meegan, C., Lichti, G., Bhat, P., et al. 2009, *The Astrophysical Journal*, 702, 791
- Norris, J. P., Bonnell, J. T., Kazanas, D., et al. 2005, *ApJ*, 627, 324, doi: [10.1086/430294](https://doi.org/10.1086/430294)
- Pe'er, A., Ryde, F., Wijers, R. A., Mészáros, P., & Rees, M. J. 2007, *The Astrophysical Journal Letters*, 664, L1
- Produit, N., Bao, T. W., Batsch, T., et al. 2018, *Nuclear Instruments and Methods in Physics Research A*, 877, 259, doi: [10.1016/j.nima.2017.09.053](https://doi.org/10.1016/j.nima.2017.09.053)
- Racusin, J., Liang, E., Burrows, D. N., et al. 2009, *The Astrophysical Journal*, 698, 43
- Racusin, J. L., Oates, S. R., Schady, P., et al. 2011, *ApJ*, 738, 138, doi: [10.1088/0004-637X/738/2/138](https://doi.org/10.1088/0004-637X/738/2/138)
- Rao, A. R., Bhattacharya, D., Bhalerao, V. B., Vadawale, S. V., & Sreekumar, S. 2017, *Current Science*, 113, 595, doi: [10.18520/cs/v113/i04/595-598](https://doi.org/10.18520/cs/v113/i04/595-598)
- Scargle, J. D., Norris, J. P., Jackson, B., & Chiang, J. 2013, *The Astrophysical Journal*, 764, 167
- Sharma, V., Bhattacharya, D., Bhalerao, V., et al. 2018, *GRB Coordinates Network*, 22694, 1
- Sharma, V., Iyyani, S., Bhattacharya, D., et al. 2020, *MNRAS*, 493, 5218, doi: [10.1093/mnras/staa570](https://doi.org/10.1093/mnras/staa570)
- . 2019, *ApJL*, 882, L10, doi: [10.3847/2041-8213/ab3a48](https://doi.org/10.3847/2041-8213/ab3a48)
- Toma, K., Sakamoto, T., Zhang, B., et al. 2009, *ApJ*, 698, 1042, doi: [10.1088/0004-637X/698/2/1042](https://doi.org/10.1088/0004-637X/698/2/1042)
- Vadawale, S., Chattopadhyay, T., Rao, A., et al. 2015, *Astronomy & Astrophysics*, 578, A73
- Vianello, G., Lauer, R. J., Younk, P., et al. 2015, *arXiv e-prints*, arXiv:1507.08343, <https://arxiv.org/abs/1507.08343>
- Watanabe, S. 2010, *Journal of Machine Learning Research*, 11, 3571
- Waxman, E. 2003, *Nature*, 423, 388, doi: [10.1038/423388a](https://doi.org/10.1038/423388a)